Editors' Suggestion

Flow characteristics around extremely low fineness-ratio circular cylinders

Masahide Kuwata,[1,2] Yoshiaki Abe,[2,*] Sho Yokota,[1] Taku Nonomura,[1] Hideo Sawada,[2]
Aiko Yakeno,[2] Keisuke Asai,[1] and Shigeru Obayashi[2]

[1]*Department of Aerospace Engineering, Graduate School of Engineering, Tohoku University, 6-3, Aoba, Aramaki, Aoba-ku, Sendai, Miyagi 980-8578, Japan*

[2]*Institute of Fluid Science, Tohoku University, 2-1-1 Katahira, Aoba-ku, Sendai, Miyagi 980-8577, Japan*

(Received 22 October 2020; accepted 22 February 2021; published 27 May 2021)

The accurate measurement of flows and aerodynamic characteristics around a bluff body has been a challenging task due to the existence of interference between the wake and mechanical model supports in wind-tunnel experiments. The present study focuses on a freestream-aligned circular cylinder with an extremely low fineness ratio (the ratio of the axial length to diameter) ranging from 0.30 to 0.50, which has never been investigated without interference from a mechanical model support. We employed a magnetic suspension and balance system to eliminate interference from the model support and measured the drag and velocity fields in the diameter-based Reynolds number between 2.0×10^4 and 7.7×10^4. As the fineness ratio decreases below 1.50, the size of the recirculation bubble increases and the velocity distribution on the central axis inside the bubble gradually converges to that of the circular disk. Furthermore, large-eddy simulations were performed in the Reynolds number of 4.0×10^4, whose drag coefficient agrees well with experiments. Based on those results, it was found that the drag coefficient monotonically converges to that of the circular disk without local maximum. This study revealed that in the low-fineness-ratio regime (0.10–0.50), a critical geometry, at which the drag coefficient shows a local maximum, does not exist in the circular cylinder. Subsequently, unsteady flow analyses were performed, where two characteristic frequencies, i.e., St = 0.05 and 0.155, were identified from power spectral densities of the drag coefficient and the pitching moment coefficient. The associated flow structures are then extracted by a phase-averaging procedure, where the phase-averaged flows with St = 0.05 represent the recirculation bubble pumping while the phase-averaged flows with St = 0.155 show nonaxisymmetric structures inside the recirculation bubble.

DOI: 10.1103/PhysRevFluids.6.054704

I. INTRODUCTION

The aerodynamic characteristics of a bluff body are related to the large-scale and complex wake structures. Studies on the relationship between the aerodynamic characteristics and wake structures are important not only for understanding their basic fluid dynamics but also for applications to practical fluid-engineering problems. However, comprehension of fluid physics around such a bluff body is a challenging issue in fluid dynamics, owing to its complexity. Thus far, flow around a circular cylinder has garnered great interest as one of the most simplified geometries which approximates a bluff body.

One of the most effective parameters that can determine the aerodynamic characteristics of a circular cylinder is a fineness ratio L/D, which is the ratio of the axial length L to the diameter D [1].

*yoshiaki.abe@tohoku.ac.jp

When the aerodynamic characteristic or flow field significantly changes at a certain fineness ratio, the corresponding shape is called a "critical geometry" [2]. A two-dimensional rectangular cylinder has a critical geometry at the fineness ratio of approximately 0.70 [2,3]. For a freestream-aligned circular cylinder, the aerodynamic drag is similarly sensitive to the fineness ratio, which are summarized in some fluid dynamic handbooks [4,5]. Roberson *et al.* [6] measured drag coefficients for a circular cylinder with various L/D through a sting-supported wind-tunnel test with different levels of inflow turbulence. Their results are well summarized in Refs. [4,7] and suggest that the trend of the drag coefficient slightly increases at $1.0 < L/D < 2.0$ as L/D decreases from 4.0 to 0.0, which implicates the existence of the critical geometry of a circular cylinder at around $1.0 < L/D < 2.0$. Note that although the corresponding data are plotted in Fig. 8 as white squares, the drag increase at $L/D \simeq 1.5$ is not apparent since Fig. 8 focuses on a smaller L/D range between 0.0 and 4.0, while Fig. 11 of Higuchi *et al.* [7] clearly shows the drag increase at $1.0 \leqslant L/D \leqslant 2.0$. However, the aforementioned experimental studies could have some uncertainty due to the mechanical supports in the wind tunnel. As the conventional model-support device (e.g., sting and strut) disturbs the wake structure and generates complex flows around the model, it is not easy to rigorously evaluate drag coefficients without the effect of support interference. Therefore, a magnetic suspension and balance system (MSBS) was utilized in our experiment to eliminate the interference from support devices. Furthermore, aerodynamic forces acting on the model can be directly evaluated from magnetic forces, where the model is magnetically supported without mechanical contact for the force measurement.

Sawada *et al.* [8] measured the drag and base-pressure coefficients of circular cylinders with $L/D = 1.27$–1.79 by using a 0.6-m MSBS at the Aeronautical Technology Directorate, Japan Aerospace Exploration Agency (JAXA). They revealed that the drag coefficient shows a local minimum at $L/D = 1.60$–1.80. Higuchi *et al.* [7] further investigated the effect of a shear layer reattachment in the corresponding fineness-ratio regime using the same MSBS. They reported that when $L/D < 1.60$, the separated shear layer which is detached from the leading edge does not reattach on the side surface of the cylinder. On the other hand, when $L/D > 1.70$, reattachment occurs, and the turbulent boundary layer is developed in the downstream. Their observations suggest that the shear-layer reattachment would characterize the flow field around the circular cylinder. Following these studies, Nonomura *et al.* [9] and Shinji *et al.* [10] studied a trend of the drag and base-pressure coefficients with $L/D = 0.50$–2.00 by using the 1-m MSBS at the Institute of Fluid Science, Tohoku University. They reported that the drag coefficient monotonically increases as L/D decreases from 1.50, and the base pressure coefficient shows the same trend as the entire drag coefficient. In other words, the base pressure is closely related to the drag coefficient at $L/D < 1.50$. Their results indicated that no critical geometry exists in the range of $L/D = 0.50$–1.50. However, the trend of the drag coefficient of a circular cylinder with $L/D \leqslant 0.50$ has never been rigorously investigated using the 1-m MSBS due to lack of accuracy in the model-position-sensing subsystem. Furthermore, wake structures of a low-fineness-ratio circular cylinder, like a circular disk, have been of interest to researchers. Berger *et al.* [11] investigated the vortex structures in the wake of a circular disk by the point cross-spectral analysis of velocity and pressure fluctuations. They defined three vortex structures which have different characteristic frequencies: recirculation bubble pumping at low frequency ($\mathrm{St} \simeq 0.05$), helical vortex structures ($\mathrm{St} \simeq 0.135$) and shear layer instability at high frequency. These vortex structures were also confirmed by the numerical simulation (see Refs. [12,13]). However, there are very few studies regarding the effect of these unsteady flow structures on the aerodynamic characteristics in particular to extremely low fineness-ratio circular-cylinder models ($L/D = 0.30$–0.50) without the effect of support interference.

Recently, a new model-position-sensing method was developed for such extremely low fineness-ratio circular-cylinder models, enabling us to conduct the MSBS experiments and measure the drag coefficient of circular cylinders with $L/D = 0.30$–0.50 by using 0.1- and 0.3-m MSBSs at Tohoku University [14]. To the authors' knowledge, this is the first study to perform MSBS experiments and measure drag coefficients of circular cylinders with $L/D \leqslant 0.50$. The associated flow characteristics were also investigated, particularly around the wake-recirculation region using particle image

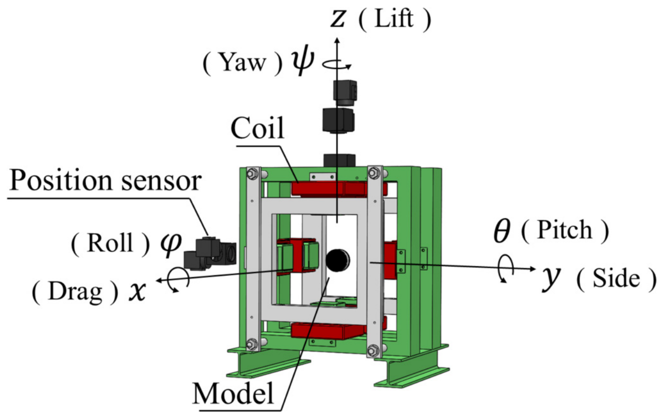

FIG. 1. Schematic of the 0.3-m MSBS and definition of the coordinate system.

velocimetry (PIV). Furthermore, large-eddy simulations (LES) of the same flow condition were conducted, which validates the experimental results. In the experiments, the Reynolds number based on the cylinder diameter (Re_D) was set to be 2.0×10^4–7.7×10^4, and L/D was ranged from 0.30 to 0.50. Here the order of the Reynolds number was the same as those employed in Sawada *et al.* [8] and Higuchi *et al.* [7] The present study details the trend of the drag coefficients of circular cylinders with $L/D \leqslant 0.50$ and the associated flow characteristics. The rest of this paper is organized as follows. Section II describes the methodologies of experiments and simulations. In Sec. III, experimental results including the trend of the drag coefficient and PIV measurement are discussed, and the simulation results support the experimental measurements. Furthermore, the unsteady flow characteristics are discussed specifically for the case of $L/D = 0.30$. Finally, Sec. IV concludes this paper.

II. ANALYSIS METHODS

A. Experiments and experimental apparatus

In this study, experiments were performed in the suction-type wind tunnel, which is called the "Tohoku University Basic Aerodynamics Research Tunnel." The wind tunnel has a closed-type test section, and the cross-sectional shape of the test section is 0.3 m × 0.3 m. The available freestream velocity ranges from 5 to 60 m/s, and the turbulence intensity is lower than 0.5%.

Figure 1 shows the 0.3-m MSBS of Tohoku University (see Ref. [15]), which we employed in the wind-tunnel testing. This MSBS is similar to that developed by Sawada *et al.* [16] and his group at JAXA. The 0.3-m MSBS consists of four subsystems: model position sensor, coils, amplifiers, and a controller.

Charge coupled device (CCD) line sensors were used for the model-position-sensing subsystem of the 0.3-m MSBS. To detect the model position, blue light-emitting diodes were used to illuminate the model surface, and the reflected model image was projected to the CCD line sensors, which were orthogonally arranged. The coil subsystem has eight electromagnets and two air-cored coils. These coils were symmetrically arranged with respect to the center of the test section. The model position and attitude can be adjusted by independently controlling the currents through each coil. The coil currents were generated from the amplifiers according to the control signal from the controlling subsystem. The controlling subsystem uses a feedback control based on the proportional-integral controller with a double-phase advancer. A target of the feedback control is the model position. The coil currents are determined by the model-position information obtained from the model-position-sensing subsystem. As the circular cylinder has an axisymmetric shape, we employed a five degrees-of-freedom control, excluding the roll angle. The entire system was synchronised at a

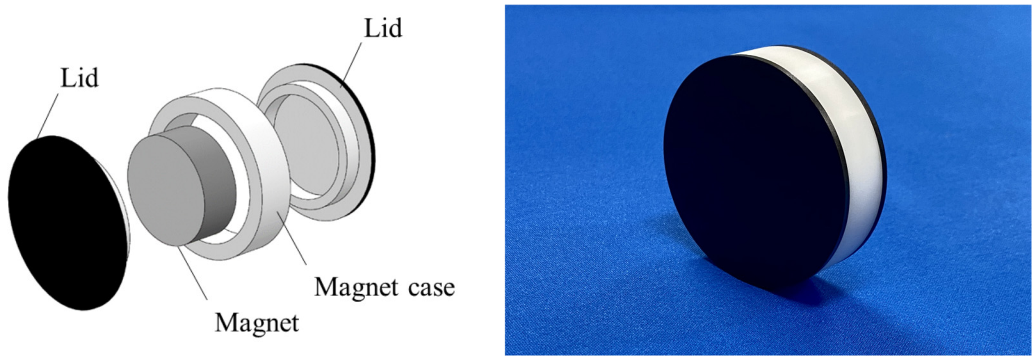

FIG. 2. Circular cylinder model with $L/D = 0.30$ (diameter 60 mm).

control frequency of 1250 Hz. During the wind-tunnel testings, the model position and coil currents were measured at the sampling rate of 1250 Hz, at which the number of data points was 9000. The measurement time was 7.2 s and approximately corresponds to 68 shedding cycles in $\mathrm{St} = 0.05$, which will be focused as a lower frequency event later, in the typical flow condition of $D = 80$ mm and $U_\infty = 15$ m/s. The time-averaged quantities are given by taking an average of entire samplings above. On the other hand, the power spectrum density (PSD) in Fig. 9 is obtained as follows: the measured samples were divided into five segments with 50% overlaps, and then a moving average was taken from fast Fourier transform (FFT) results of each segment, i.e., so-called the Welch's method. Therefore, the number of samplings for the PSD is 2998 in terms of a FFT process, which approximately corresponds to 23 shedding cycles in $\mathrm{St} = 0.05$ of the lower frequency event. The number of samplings above are considered sufficient for the discussion in this paper.

Figure 2 describes the structure of the circular cylinder model, composed of a neodymium magnet and three nonmagnetized parts made of polyoxymethylene. The lids were painted in black to alleviate detection of the model position by the CCD line sensor. The width of the lid, which is the length in the cylindrical axis direction of the lid, was changed according to L/D. This is because the length of the magnet case colored in white needs to be fixed so that the same configuration can be employed in the CCD line sensor for different fineness ratios.

In the experiment, we used L/D ranging from 0.30 to 0.50 and cylindrical models with two different diameters. The model with 60-mm diameter had three fineness ratios ($L/D = 0.30$, 0.40, and 0.50), and the blockage ratio to the cross-sectional area of the test section was 3.1%. The L/D values for the model with an 80-mm diameter was 0.30, 0.35, 0.38, and 0.45, and the blockage ratio was 5.6%. As the blockage effect on aerodynamic-force measurement should be considered, the drag coefficients measured in the experiment were corrected by Maskell's blockage correction method (see Ref. [17]). The correction reduces the drag coefficient by 5.1% and 18.5% for each of the models.

The freestream velocity was varied from 5 to 15 m/s, and the model was fixed in the center of the test section. The model attitude was adjusted to be parallel to the freestream. When the model was magnetically supported in the airflow of 15 m/s, the model-position errors in the translational direction and the pitch and yaw angles were controlled to be within ± 0.15 mm and $\pm 0.25^\circ$, respectively. Although no quantitative evaluation has been performed on evaluating the effect of unsteadiness due to the model vibration, the model-position errors above are sufficiently small [$\mathcal{O}(0.1\%)$ of the model diameter], and hence it is expected that the measurements of the aerodynamic load and PIV are not affected by the model vibration in terms of their unsteady characteristics.

The relationship between the coil current and external load was calibrated by applying known loads to the magnetically supported model by using a pulley, a thread, and weights to measure the aerodynamic forces from the coil currents. Throughout this study, the reference area of drag coefficient C_D is the cross-sectional area of the circular cylinder. The uncertainty of the coefficient

$\Delta C_D/C_D$ was evaluated from force-calibration error $\Delta F/F$, dynamic pressure-measurement error $\Delta q_{net}/q_{net}$, and model dimensional error $\Delta S/S$, as follows:

$$\left(\frac{\Delta C_D}{C_D}\right)^2 = \left(\frac{\Delta F}{F}\right)^2 + \left(\frac{\Delta q_{net}}{q_{net}}\right)^2 + \left(\frac{\Delta S}{S}\right)^2, \tag{1}$$

where $\Delta F/F$ is calculated from the full-scale error of force calibration; $\Delta q_{net}/q_{net}$ was estimated from the performance of the digital manometer (Cosmowave Technology, DM-3501 range 500 pa, $\pm 0.15\%$ of F.S.) by measuring the differential pressure between the wind-tunnel nozzle; and $\Delta S/S$ is the error in the cross-sectional area of the model.

For the PIV measurement, the laser system is a dual head laser system using Nd: YLF (Litron Lasers, LDY 303 PIV, wavelength 527 nm) with the maximum pulse energy of 20 mJ/pulse at a repetition rate of 1 kHz. The high-speed camera (Phantom v611, Vision Research) comprises a 1280×800 CMOS sensor with 20 μ m pixel size. The seeding particles were made of the dioctyl sebacate and the particle size was approximately 1 μm [18]. In the PIV measurement, a buffer tank stored the seed particles produced by the Laskin nozzle, and then the particles were inserted into the wind tunnel from the upstream. The laser light source was installed outside the test section at the downstream side and the laser light sheet was placed in the plane parallel to the freestream, including the central axis of the circular cylinder. The camera was located between the coils of the MSBS, and was used to acquire the two-component velocity field around the model. The MSBS, laser system, and high-speed camera were synchronized using a timing hub. The framing rates for both camera and pulse laser were set at 200 or 300 Hz and 400 or 500 Hz in the cases of models with diameters of 60 and 80 mm, respectively. In contrast, 2600 pairs of images were typically acquired. The data acquisition and post processing were performed using the commercial PIV software (Dantec, Dynamic Studio). In addition, PIV uncertainty analysis based on the method proposed by Charonko and Vlachos was conducted to specify the measurement errors [19] before the moving average procedure. With regard to the time response of the particle, the Stokes number of PIV particle was estimated to be 5.20×10^{-4} based on the freestream velocity, and the density and the diameters of the particles, and therefore, the PIV particle was concluded to follow the flow motion. In addition, more details frequency response analysis based on the previous study [20] was conducted and the results showed that the PIV particle has time response characteristics that are sufficient for the discussion of unsteady behavior of flow up to the Nyquist frequency of the measurement, although the details of the analysis are omitted in this paper for brevity.

B. Computational conditions and methods

In the numerical simulation, Re_D was fixed at 4.0×10^4 and circular cylinders with $L/D =$ 0.10–0.50 were simulated to validate the experimental data. In the present study, flows over the circular cylinder were analyzed using LES based on the three-dimensional compressible Navier-Stokes equations. An in-house fluid dynamic solver called "LANS3D" [21] was employed; the code has been applied to various practical fluid problems (e.g., Refs. [22,23]), and the applicability of the code to unsteady turbulent simulations has been sufficiently validated. The governing equations are expressed in the body-fitted coordinate system, and spatial derivatives of the convective and viscous terms, coordinate transformation metrics and Jacobian (see Ref. [24]) are evaluated by a sixth-order compact scheme with a sixth-order spatial filtering with a filtering coefficient 0.475 (see Ref. [25]). Such a high-order low-pass filter selectively damps only poorly resolved high-frequency waves, and acts as an alternative of a sub-grid-scale model; the present approach is called an implicit LES. The time integration was approximated by the second-order backward difference scheme, and the lower-upper symmetric alternating direction implicit and symmetric Gauss–Seidel method was employed with five subiterations in each time step. The time-step size was normalized by 0.0005 with respect to the sound speed and cylinder diameter, and the maximum Courant number was 3.01. The Mach number was set at 0.2 so that the compressible effect is negligible [22]. At the outflow boundary, all variables were extrapolated from one point inside the boundary. Moreover, a

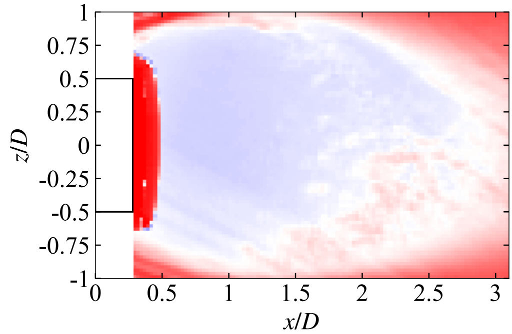

FIG. 3. RMS values of PIV measurement uncertainty in the averaged flow fields for $L/D = 0.30$ at $\mathrm{Re}_D = 5.9 \times 10^4$ with the model diameter of $D = 60$ mm.

no-slip adiabatic condition was adopted on the cylinder surface. A cylindrical grid was used around the cylinder with the inflow and outflow boundaries located at 25 and 35 times the diameter away from the leading edge, respectively. The outer boundary in the radial direction was set to be 30 times the diameter length from the central axis. The zonal grid approach [26] was adopted so that a singularity on the cylindrical axis could be avoided. The wall-normal grid spacing at the front surface was $0.045/\sqrt{\mathrm{Re}_D}$, which sufficiently resolves the laminar boundary layer before separation at the leading edge. In addition, the separated shear layer in the vicinity of the leading edge was resolved using 160 grid points in the wall normal direction. The number of grid points was 351, 201, and 751 in the radial, azimuthal, and flow directions, respectively. The simulation impulsively started with the uniform flow and continued while the freestream passed through 33 times the length of the cylindrical diameter (i.e., 33 flows through duration) to reach the quasisteady state. Then a time average was taken for 10 flows through duration after 34 flow passes from the start.

III. RESULTS AND DISCUSSIONS

A. Time-averaged streamwise velocity field in the wake measured using PIV

Figure 3 represents the root-mean-square (RMS) values of the PIV measurement uncertainty in the averaged flow fields for $L/D = 0.30$ at $\mathrm{Re}_D = 5.9 \times 10^4$ with the model diameter of $D = 60$ mm. In Fig. 3, the origin of the coordinate system is defined as the center of the front surface. The x and z axes are parallel and perpendicular to the freestream direction, respectively. The uncertainty is lower than 0.07702% of the freestream velocity U_∞, which is maximized behind the cylinder and is kept lower in the most part of the recirculation region. The analysis of this study is mainly based on the mean velocity field particularly in the recirculation region, and thus, the current measurement error is sufficiently small.

Figure 4 shows the time-averaged streamwise velocity field for $L/D = 0.30$–1.50. The contour and streamline of the models with $L/D = 0.30$–0.50 were obtained through experiments, while those of the other models (i.e., $L/D = 1.00, 1.25, 1.50$) were reproduced using the data obtained from Yokota *et al.* [15]. The mean velocity components, (u, w), were normalized by the freestream velocity U_∞ and correspond to (x, z) directions, respectively.

Figure 4 shows that the large-scale recirculation bubble behind the cylinder increases as L/D decreases from 1.50. Moreover, a pair of counter-rotating-recirculation zones was formed in the wake region in this plane, regardless of the L/D value.

Figures 5(a) and 5(b) show the velocity profiles on the central axis of a circular cylinder and in the z/D direction at $x/D = 1.50$, respectively. Figure 5(a) illustrates that the reverse velocity

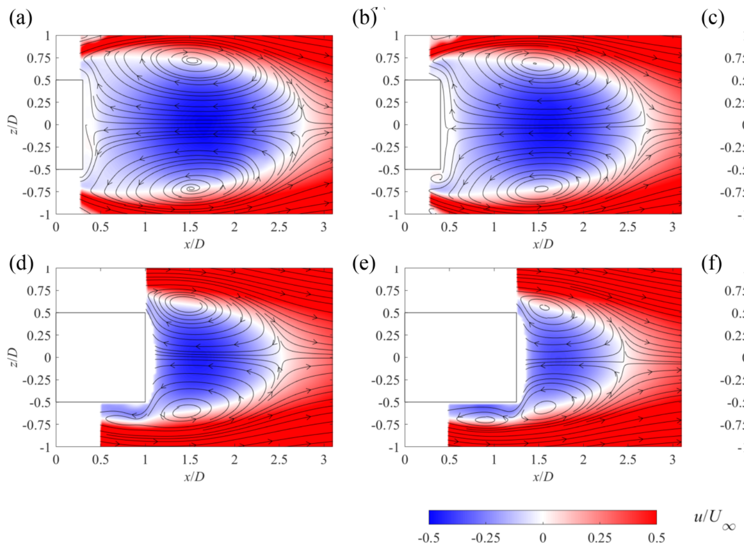

FIG. 4. Mean velocity field of the streamwise component, u/U_∞: (a) $L/D = 0.30$, (b) $L/D = 0.40$; (c) $L/D = 0.50$, (d) $L/D = 1.00$; and (e) $L/D = 1.25$, (f) $L/D = 1.50$. [(a)–(c)] Present study $\mathrm{Re}_D = 5.9 \times 10^4$ with the model diameter of $D = 60$ mm; [(d)–(f)] reprocessed data from the previous study by Ref. [15] at $\mathrm{Re}_D = 6.7 \times 10^4$).

on the central axis achieves local maximum at $x/D \approx 1.50$ and slows down when approaching the rear surface of the cylinder. The maximum reverse velocity inside the bubble increases, and then converges to approximately -0.50 with decrease in L/D. In addition, the velocity distribution was determined to be axisymmetric with respect to the central axis, as shown in Fig. 5(b). When L/D decreases, the flow velocity profile inside the recirculation bubble changes and gradually converges to that of the circular disk (i.e., $L/D = 0.0$).

Figure 6 summarizes the characteristic length scales relevant to the recirculation region. The length of the recirculation region, L_r/D, which is defined as the distance between the rear surface and the stagnation point on the cylinder axis, monotonically increases and the stagnation point recedes to downstream direction, with decreasing L/D. Note that the stagnation point is defined as the xz location in Fig. 4 where the two-dimensional time-averaged velocity magnitude, $\sqrt{u^2 + w^2}$, is

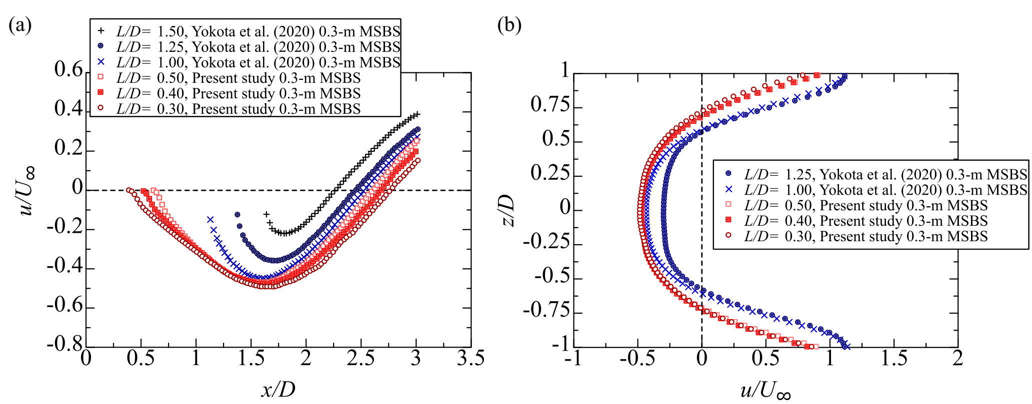

FIG. 5. Mean velocity profiles of circular cylinders (a) at the central axis, $z/D = 0.0$; (b) $x/D = 1.50$ (present study at $\mathrm{Re}_D = 5.9 \times 10^4$ with model diameter $D = 60$ mm and [15] at $\mathrm{Re}_D = 6.7 \times 10^4$).

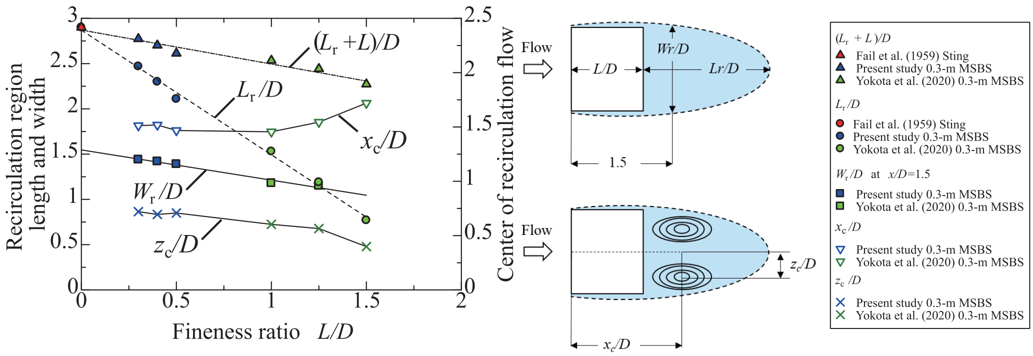

FIG. 6. Characteristics of the recirculation bubble: Recirculation region length L_r/D, width W_r/D at $x/D = 1.5$, and center of recirculation flow $(x_c/D, z_c/D)$ (Ref. [27], $\mathrm{Re}_D = 4.1 \times 10^5$; present study, $\mathrm{Re}_D = 5.9 \times 10^4$ with model diameter $D = 60$ mm; Ref. [15], $\mathrm{Re}_D = 6.7 \times 10^4$).

minimized. L_r/D and $(L_r + L)/D$ change linearly with respect to L/D, where the gradients of L_r/D and $(L_r + L)/D$ with respect to L/D are estimated as -1.38 and -0.38, respectively. Similarly, the width of the recirculation region, W_r/D, which is defined as the distance between the inflection points of u/U_∞ in the z/D direction at $x/D = 1.5$, increases with the decrease in L/D, where its gradient with respect to L/D is -0.33. Furthermore, the results revealed that the length and width of the recirculation bubble (L_r/D and W_r/D, respectively) continue expanding while the center of the recirculation flow $(x_c/D, z_c/D)$ converges with decrease in L/D. Note that the data of the plot at $L/D = 0.0$ in Fig. 6 were measured through the sting-supported wind-tunnel testing by using pitot-static tubes [27], and the plot shows good agreement with the MSBS data extrapolated to $L/D = 0.0$.

As such, in the case of a lower fineness ratio, the mean velocity characteristics behind the cylinder indicate that the size of the recirculation bubble expands. In contrast, the velocity distribution inside the bubble, including $(x_c/D, z_c/D)$, converges to that of the circular disk. A similar convergence behavior with respect to the decrease in L/D is observed for the drag coefficients in Figure 8, where the base-pressure distribution of the cylinder with $L/D \leqslant 0.50$ is expected to be approximately constant regardless of L/D.

B. Trend of drag coefficients with respect to fineness ratios

Figure 7 shows the effect of the Reynolds number on drag coefficient C_D of a circular cylinder with $L/D = 0.30$–0.50. In addition, the figure shows the uncertainty of experimental results estimated through Eq. (1). Although the uncertainty is larger in the lower Re_D conditions (i.e., $\mathrm{Re}_D < 4.0 \times 10^4$), the result indicates that the effect of the Reynolds number on C_D is smaller for $\mathrm{Re}_D = 2.0 \times 10^4$–$7.7 \times 10^4$ than that when changing L/D. Furthermore, the drag coefficient becomes almost constant (i.e., $C_\mathrm{D} \approx 1.17$) regardless of the change of L/D from 0.30 to 0.50. Higuchi *et al.* [7] investigated the effect of the Reynolds number on C_D of the longer circular cylinder with $L/D = 4.13, 6.13$, and 8.13 for $\mathrm{Re}_D = 6.0 \times 10^4$–$1.0 \times 10^5$, and concluded the effect to be negligible in the case of a large L/D. Therefore, when a cylinder is arranged parallel to the freestream, the Reynolds-number dependence on C_D was not observed in the range we investigated, regardless of the value of L/D.

The effects of the fineness ratio on the drag and base-pressure coefficient of circular cylinders at $\mathrm{Re}_D = 10^4$–10^5 are summarized in Fig. 8. The drag coefficient measured using the 0.3-m MSBS and the drag and base-pressure coefficients estimated through LES are plotted with the results of previous studies. Figure 8 shows that C_D of the sting-supported experiment in Ref. [6] and the LES results agree well with the value obtained through the MSBS experimental data. Moreover, the

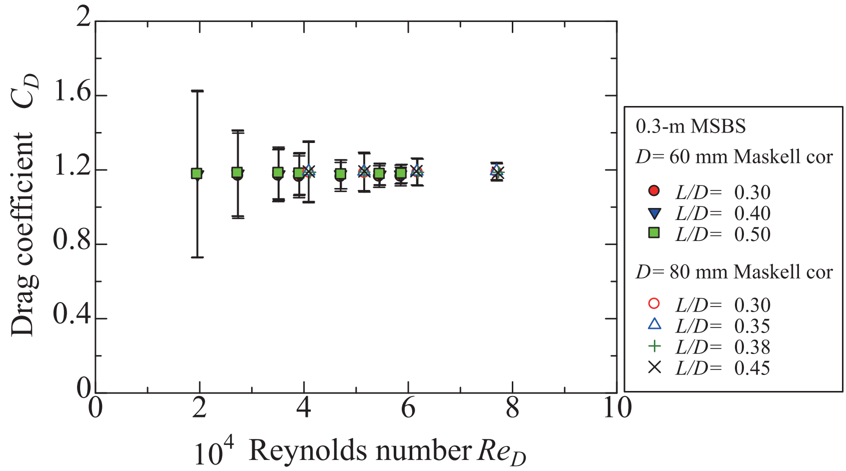

FIG. 7. Drag coefficients versus Reynolds number of circular cylinders with fineness ratios of 0.30–0.50, measured using the 0.3-m MSBS.

base-pressure coefficient, $-C_{pb}$, of $L/D \leqslant 0.50$ was found to be approximately constant, similar to C_D. Therefore, the LES result suggests that the pressure drag at the base of the cylinder does not drastically change with L/D in the case of the extremely low L/D conditions.

The trend of the drag coefficient with respect to the fineness ratio could be classified into three regimes: $L/D > 1.50$; $0.50 < L/D \leqslant 1.50$; and $L/D \leqslant 0.50$. First, Higuchi *et al.* [7] suggested that the separated shear layer reattaches onto the side surface of the cylinder and the base pressure is nearly constant at $L/D \gtrapprox 1.70$. In this regime, C_D slightly decreases with decreasing L/D because the viscous drag decreases with the decrease in the reattached flow region on the side surface. Second, the separated shear layer detaches from the rear edge and forms a large-scale recirculation bubble in the case of $0.50 < L/D \leqslant 1.50$. In this regime, the size of the recirculation bubble increases along with the reverse velocity inside the bubble with decreasing L/D (see Figs. 5 and 6). This trend is related to the enhancement of reverse flow near the rear surface due to the decrease in the base pressure. The decrease in the base pressure leads to the increase of C_D as L/D decreases.

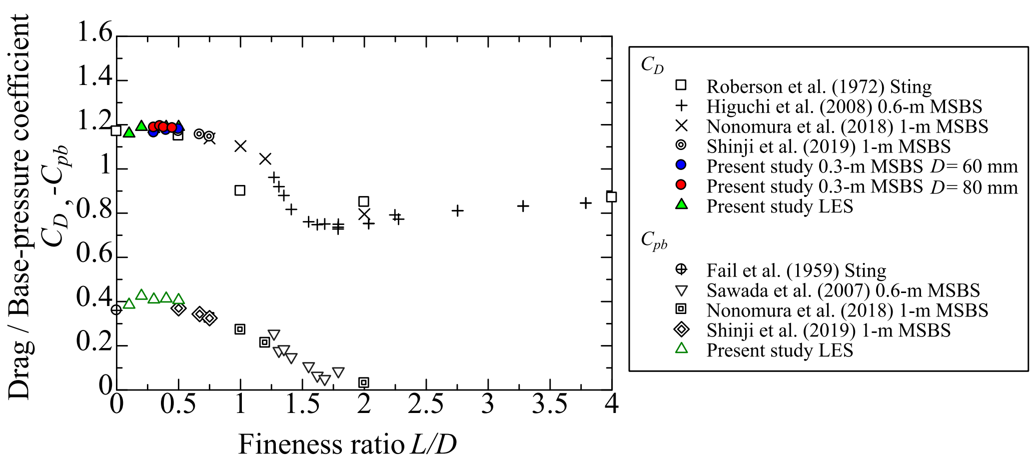

FIG. 8. Effects of fineness ratio on drag and base-pressure coefficient of circular cylinder at $\mathrm{Re}_D = 10^4$–10^5 (present study; $\mathrm{Re}_D = 5.9 \times 10^4$ and 7.7×10^4 for models with diameter $D = 60$ and 80 mm, respectively).

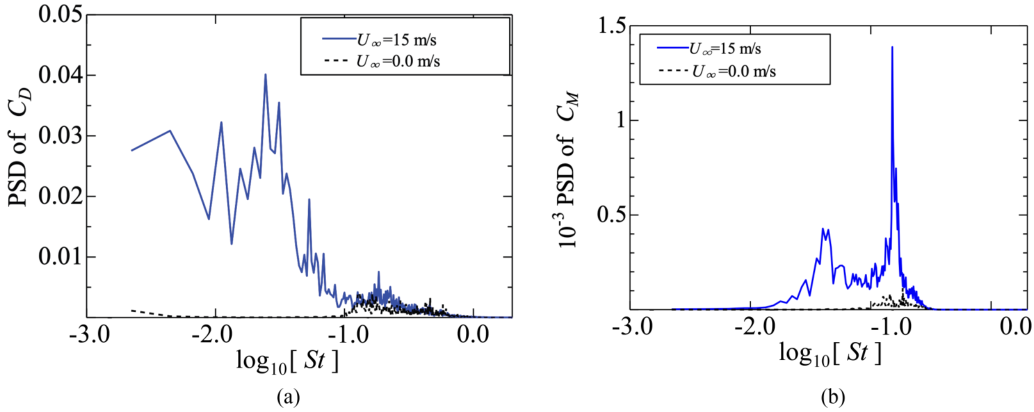

FIG. 9. PSDs of (a) the drag coefficient C_{D} and (b) the pitching moment coefficient C_{M} in the $L/D = 0.30$ case at $\mathrm{Re}_D = 7.7 \times 10^4$ with the model diameter of $D = 80$ mm.

Finally, Figs. 5 and 6 show that the length and width of the recirculation region continue increasing in the case of $L/D \leqslant 0.50$, while the streamwise velocity profile inside the bubble converges smoothly. Considering the trend of the characteristic of the recirculation bubble and drag coefficient, the base pressure is also expected to be constant in $L/D \leqslant 0.50$; this is supported by the LES estimation of $-C_{pb}$. Therefore, C_{D} became almost constant and monotonically converged to that of the circular disk. As such, there appears to be no critical geometry, at which C_{D} drastically changes in the case of $L/D \leqslant 0.50$.

C. Unsteady flow characteristics in recirculation bubbles

The blue lines in Fig. 9 show the PSDs of the drag coefficient C_{D} and the pitching moment coefficient C_{M} in the $L/D = 0.30$ case at $\mathrm{Re}_D = 7.7 \times 10^4$ with the model diameter of $D = 80$ mm. The black lines correspond to those in a quiescent condition that are generated by errors in the measurement, sensing, and control of the model. Comparison of the blue and black lines shows that errors (colored in black) are sufficiently smaller than signals obtained in the operating condition (colored in blue). Figure 9(a) shows the PSD has a broad peak around $\mathrm{St} = 0.03$–0.05. This low-frequency peak approximately corresponds to the recirculation-bubble-pumping frequency of a circular disk, i.e., $\mathrm{St} = 0.05$, as reported in Berger *et al.* [11]. On the other hand, Fig. 9(b) shows two distinct peaks at $\mathrm{St} \simeq 0.05$ and $\mathrm{St} \simeq 0.155$. The lower frequency of $\mathrm{St} \simeq 0.05$ corresponds to the characteristic frequency observed in the PSD of C_{D}, i.e., the bubble-pumping frequency, while the higher-frequency peak at $\mathrm{St} \simeq 0.155$ is close to that reported as the helical vortex structures in Yang *et al.* [12,13]. The recirculation-bubble-pumping motion mainly involves an axisymmetric flow structure, thereby strongly affecting the force coefficient in the streamwise direction. Meanwhile, the pitching moment can be affected by a nonaxisymmetric force acting on the cylinder, and thus, the frequency of $\mathrm{St} \simeq 0.155$ would suggest a nonaxisymmetic flow motion in the recirculation bubble. The associated flow structures will be extracted by means of a phase-averaging procedure in the next subsection.

Figure 10 shows phase-averaged flow fields of $\mathrm{St} = 0.05$ and 0.155, that were identified as characteristic frequencies in the PSD of aerodynamic coefficients. The phase decomposition for an instantaneous flow quantity $f(t)$ is described as $f(t) = \overline{f} + f'(t) = \overline{f} + \tilde{f}_\varphi + f''(t) = \langle f \rangle_\varphi + f''(t)$, where $\overline{f}$, $\tilde{f}_\varphi$, and $f''(t)$ represent an entire time-averaged, phase fluctuation, and turbulent fluctuation quantities, respectively. Given St, the phase-averaged flow quantity $\langle f \rangle_\varphi$ is defined for a

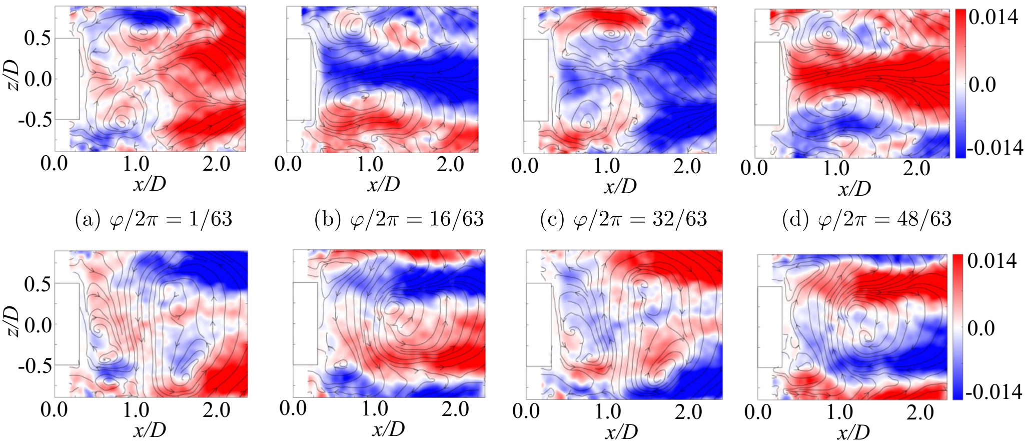

(a) $\varphi/2\pi = 1/63$ (b) $\varphi/2\pi = 16/63$ (c) $\varphi/2\pi = 32/63$ (d) $\varphi/2\pi = 48/63$

(e) $\varphi/2\pi = 1/20$ (f) $\varphi/2\pi = 5/20$ (g) $\varphi/2\pi = 10/20$ (h) $\varphi/2\pi = 15/20$

FIG. 10. Phase-averaged flow fields based on St = 0.05 [in (a)–(d)] and St = 0.155 [in (e)–(h)]. Blue to red contour colors represent the phase fluctuation $\tilde{u}_\varphi/U_\infty$, and black lines represent streamlines calculated from the phase-averaged velocity field ($\langle u\rangle_\varphi$, $\langle w\rangle_\varphi$).

discrete set of φ in $0 \leqslant \varphi \leqslant 2\pi$ as follows:

$$\langle f\rangle_\varphi = \frac{1}{N_{\mathrm{St}}}\sum_{n=1}^{N_{\mathrm{St}}} f(t_n + T\varphi/2\pi), \quad (T = 1/\mathrm{St}, \quad 0 \leqslant \varphi < 2\pi), \tag{2}$$

where t_n is defined to be a trigger timing when the nth flow event associated with the targeted St starts and is determined as follows. First, a band-pass filter of the targeted St is applied to the velocity fluctuation at $(x/D, z/D) = (2.0, 0.0)$ in the recirculation bubble, which generates a reference signal representing unsteady flow motion associated with the targeted St. Then, t_n is determined to be the timings when the reference signal exceeds an averaged value of its maximum and minimum values, resulting in N_{St} samples for each phase. Finally, the phase fluctuation is computed as $\tilde{f}_\varphi = \langle f\rangle_\varphi - \overline{f}$. Figure 10 shows the blue to red contours of the phase fluctuation $\tilde{u}_\varphi/U_\infty$ with streamlines of the phase-averaged field ($\langle u\rangle_\varphi$, $\langle w\rangle_\varphi$). Figures 10(a)–10(d) and Figs. 10(e)–10(h) correspond to those in the St = 0.05 and 0.155 cases, respectively. In the St = 0.05 case [Figs. 10(a)–10(d)], a pair of counter-rotating flows expands and shrinks repeatedly in the x direction. Furthermore, the flow structure is approximately symmetrical with respect to the xy plane throughout the phases, and thus, the corresponding unsteady force that acts on the cylinder base would also be symmetrical about the y axis. Therefore, this symmetrical flow motion causes the broad peak around St = 0.05 in the PSD of C_{D}, which can be identified as the recirculation bubble pumping. Meanwhile, in the St = 0.155 case [Figs. 10(e)–10(h)], flow structures are not symmetrical about the xy plane throughout the phases. The phase-averaged field at $\varphi/2\pi = 1/20$ has an anticlockwise rotating structure at $1.25 \leqslant x/D \leqslant 2.25$ as well as the associated secondary flow with a clockwise rotating structure just behind the cylinder at $0.25 \leqslant x/D \leqslant 1.00$, that are both nonsymmetrical about the xy plane. The similar nonsymmetrical flow structures are observed in the other phases, and thus, the associated unsteady force acting on the cylinder base would be also nonsymmetrical in the y axis. Indeed, the corresponding St = 0.155 is amplified only in the PSD of C_{M}, which is not observed in the PSD of C_{D}. A more detailed analysis would be required for identification of the three-dimensional flow structures, and thus, it cannot be concluded that the present characteristic frequency of St = 0.155 corresponds to the helical vortex structures as reported in Refs. [12,13]. Nevertheless, it is noteworthy that the associated phase-averaged structures in St = 0.05 and 0.155 are clearly different in terms of the symmetricity about the xy plane, which is consistent with the difference in the PSD of C_{D} and C_{M} considering the force acting on the cylinder base. Finally, although time-averaged C_D of the LES results agrees well with that of the experimental results, the phase-averaging analysis for the LES data cannot be performed due to the limited simulation time in which the low frequency events such as St = 0.05 and 0.155 are not sufficiently captured. This is due to the limit of computational resources available for the present study, and therefore, the phase-averaging analysis based on the LES data is left for the future study.

IV. CONCLUSIONS

The drag coefficients and velocity field in the wake of a freestream-aligned circular cylinder with fineness ratio, $L/D \leqslant 0.50$ were investigated. The MSBS was utilised in the wind-tunnel testing, and the support interference was eliminated. The measured drag coefficient shows good agreement with that obtained through a previous sting-supported wind-tunnel testing. PIV was used to analyze the aerodynamic drag and obtain the mean velocity field in the wake. LESs were performed for cross-validation of the experimental data, and the drag and base-pressure coefficients were estimated from the simulation results. The drag coefficient of $L/D = 0.30$–0.50 calculated by the LES agreed well with that obtained through MSBS testings. The recirculation bubble formed behind the circular cylinder continued to expand when the fineness ratio decreased from 1.50. On the other hand, the streamwise velocity profile inside the recirculation bubble gradually converged to that of the circular disk. Moreover, the length and width of the recirculation bubble are linearly increased as the fineness ratio decreases, which converges to that of the circular disk. In contrast, the center of the recirculation bubble moves nonlinearly and approaches to constant values as the fineness ratio decreases. The MSBS-based aerodynamic force measurement revealed that the drag coefficient of the fineness ratio lower than 0.50 becomes almost constant regardless of the change in the fineness ratio. Considering the characteristics of the mean velocity field and drag coefficient, the base pressure is expected to be approximately constant in the lower-fineness-ratio regime. The LES-estimated base pressure was also approximately constant, which supports the experimental observation mentioned earlier. As a consequence, the velocity distribution and drag coefficient of the circular cylinder with respect to the fineness ratio of less than 0.50 do not show a critical geometry and smoothly converge to those of the circular disk. Unsteady characteristics of the aerodynamic coefficients are then investigated for the $L/D = 0.30$ case, where two frequencies, i.e., St = 0.05 and 0.155, were identified from the PSD of C_D and C_M. The associated flow structures for these frequencies are extracted using phase-averaging procedure. The phase-averaged flow with St = 0.05 represents a pair of oscillatory counter-rotating flow inside the recirculation bubble, which produces a *xy*-symmetric force acting on the cylinder base, thereby resulting in the PSD of C_D with a peak at St = 0.05. Meanwhile, the phase-averaged flow with St = 0.155 shows nonaxisymmetric flows behind the cylinder, and thus, the peak of St = 0.155 only appears in C_M. Therefore, the flow motion of St = 0.05 would correspond to the recirculation bubble pumping, whereas we need a more investigation to identify the three-dimensional flow structure associated with St = 0.155 which is clearly nonaxisymmetric to the *x* axis as opposed to the bubble pumping structures. As such, a series of drag coefficient measurements with different fineness ratios contribute to the improvement of shape-dependence study for the aerodynamic characteristics of an axisymmetric three-dimensional bluff body. Specifically, this study revealed for the first time the drag coefficients in the low-fineness ratio circular cylinders ($L/D = 0.30$–0.50), which involves a separated shear layer that does not reattach onto the side surface. Furthermore, the steady and unsteady flow structures inside the recirculation bubble were extracted by PIV measurements and phase-averaging procedures.

ACKNOWLEDGMENT

This work was supported by Japan Society for the Promotion of Science, KAKENHI, Grant No. 18H03809. The authors are grateful of the detailed advises on the PIV-experiment setup by Dr. Yuta Ozawa of Tohoku University.

[1] S. F. Hoerner, *Fluid Dynamic Drag* (Hoerner Fluid Dynamics, US, 1965).
[2] H. Nakaguchi, K. Hashimoto, and S. Muto, An experimental study on aerodynamic drag of rectangular cylinders, Acad. J. JSASS **16**, 1 (1968).
[3] P. W. Bearman and D. W. Trueman, An investigation of the flow around rectangular cylinders, Aeronaut. Q. **23**, 229 (1972).
[4] T. C. Crowe, D. F. Elger, B. C. Williams, and J. A. Roberson, Drag and lift, in *Engineering Fluid Mechanics*, 9th ed. (Wiley, US, 2009).
[5] R. D. Blevins, Fluid dynamic drag, in *Applied Fluid Dynamics Handbook* (Krieger, Malabar, FL, 1984).
[6] J. A. Roberson, C. Y. Lin, G. S. Rutherford, and M. D. Stine, Turbulence effect on drag of sharp-edged bodies, J. Hydraul. Div. **98**, 1187 (1972).
[7] H. Higuchi, H. Sawada, and H. Kato, Sting-free measurements on a magnetically supported right circular cylinder aligned with the free stream, J. Fluid Mech. **596**, 49 (2008).
[8] H. Sawada, T. Kunimasu, S. Suda, T. Misunou, and H. Higuchi, Drag and base pressure of axial cylinder at fineness ratios from 1.27 to 1.79, J. Wind Eng., J. Aerodynam. Wind Eng. **32**, 113 (2007) [in Japanese].
[9] T. Nonomura, K. Sato, K. Fukata, H. Nagaike, H. Okuizumi, Y. Konishi, K. Asai, and H. Sawada, Effect of fineness ratios of 0.75-2.0 on aerodynamic drag of freestream-aligned circular cylinders measured using a magnetic suspension and balance system, Exp. Fluids, **59**, 77 (2018).
[10] K. Shinji, H. Nagaike, T. Nonomura, K. Asai, H. Okuizumi, Y. Konishi, and H. Sawada, Aerodynamic characteristics of low-fineness-ratio freestream-aligned cylinders with magnetic suspension and balance system, AIAA J. **58**, 3711 (2020).
[11] E. Berger, D. Scholz, and M. Schumm, Coherent vortex structure in the wake of a sphere and a circular disk at rest and under forced vibrations, J. Fluids Struct. **4**, 231 (1990).
[12] J. Yang, M. Liu, G. Wu, and X. Zhang, Numerical study on coherent structure behind a circular disk, J. Fluids Struct. **51**, 172 (2014).
[13] J. Yang, M. Liu, G. Wu, G. Liu, and X. Zhang, Low-frequency characteristics in the wake of a circular disk, Phys. Fluids **27**, 064101 (2015).
[14] M. Kuwata, S. Yokota, H. Sawada, Y. Abe, A. Yakeno, T. Nonomura, K. Asai, and S. Obayashi, Drag coefficients of circular cylinders with fineness ratio of less than 0.50 measured by 0.1 and 0.3 m magnetic suspension and balance systems, *AIAA Scitech 2020 Forum* (AIAA Inc., 2020) AIAA Paper 2020-1325, doi:10.2514/6.2020-1325.
[15] S. Yokota, T. Ochiai, Y. Ozawa, T. Nonomura, and K. Asai, Analysis of unsteady flow around an axial circular cylinder of critical geometry using combined synchronous measurement in magnetic suspension and balance system, Exp. Fluids **62**, 15 (2021).
[16] H. Sawada, S. Suda, and T. Kunimasu, NAL 60cm magnetic suspension and balance system, *Congress of International Council of the Aeronautical Sciences* (JAXA, the Institute of Space Technology and Aeronautics (ISTA), Japan, 2004).
[17] E. C. Maskell, A Theory of the Blockage Effects on Bluff Bodies and Stalled Wings in a Closed Wind Tunnel (Aeronautical Research Council, London, 1963).
[18] C. Kähler, B. Sammler, and J. Kompenhans, Generation and control of tracer particles for optical flow investigations in air, Exp. Fluids **33**, 736 (2002).
[19] J. J. Charonko and P. P. Vlachos, Estimation of uncertainty bounds for individual particle image velocimetry measurements from cross-correlation peak ratio, Meas. Sci. Technol. **24**, 065301 (2013).
[20] A. Hjelmfelt and L. Mockros, Motion of discrete particles in a turbulent fluid, Appl. Sci. Res. **16**, 149 (1966).
[21] K. Fujii, Development an accurate and efficient method for compressible flow simulation - an example of CFD in aeronautics, in *Proceedings of the 5th International Conference on Numerical Ship Hydrodynamics* (National Academy of Sciences, US, 1989).

[22] K. Asada, Computational Analysis of the Flow Fields Induced by a DBD Plasma Actuator toward Separated-Flow Control, Ph.D. thesis, The University of Tokyo (2014).

[23] H. Aono, H. Fukumoto, Y. Abe, M. Sato, T. Nonomura, and K. Fujii, Separated flow control of small horizontal-axis wind turbine blades using dielectric barrier discharge plasma actuators, Energies **13**, 1218 (2020).

[24] Y. Abe, N. Iizuka, T. Nonomura, and K. Fujii, Geometric interpretations and spatial symmetry property of metrics in the conservative form for high-order finite-difference schemes on moving and deforming grids, J. Comput. Phys. **260**, 163 (2014).

[25] D. V. Gaitonde and M. R. Visbal, Padeé-type higher-order boundary filters for the Navier-Stokes equations, AIAA J. **38**, 2103 (2000).

[26] K. Fujii, Unified zonal method based on the fortified solution algorithm, J. Comput. Phys. **118**, 92 (1995).

[27] R. Fail, J. A. Lawford, and R. C. W. Eyre, Low-speed experiments on the wake characteristics of flat plates normal to an air stream, Aeronautical Research Council Reports and Memoranda No. 312 (Aeronautical Research Council, 1957).